Vibrational spectroscopy

4.6 Vibrational spectroscopy

Lorenzo Mino[1], Luisa Mandrile[2], Luca Iannarelli[2], Chiara Portesi[2], Gianmario Martra[1], Andrea Mario Rossi[2]

[1]Department of Chemistry and NIS Centre, University of Torino, via Giuria 7, Torino, Italy
[2]Division of Quantum Metrology and Nanotechnologies, Istituto Nazionale di Ricerca Metrologica, Strada delle Cacce 91, Torino, Italy

Abstract: In this chapter, starting from the basic concepts of vibrational spectroscopy, we discuss the potential and limitations of IR and Raman techniques applied to nanoparticles. We describe the experimental setups and the sample preparation procedures, discussing also the metrological aspects. Finally, selected case studies of characterization of oxide nanoparticles are presented.

Key Words: IR spectroscopy, probe molecule, surface hydration, Lewis acidity, Raman microscopy, TiO_2

List of abbreviations and acronyms

ATR: Attenuated Total Reflection
CA: Contact Angle
CCD: Charge Coupled Device
DI H_2O: De-Ionized Water
DLS: Dynamic Light Scattering
DRIFTS: Diffuse Reflectance Infrared Fourier Transform Spectroscopy
FT-IR: Fourier-Transform Infrared (spectroscopy)
IRE: Internal Reflection Element
LDA: Linear Discriminant Analysis
NIST: National Institute of Standard and Technology
NP: Nanoparticle
PLS: Partial Least Squares
PTB: Physikalisch-Technische Bundesanstalt
RT: Room Temperature
SRM: Standard Reference Material

4.6.1 Introduction

Since the discovery of infrared radiation, two centuries ago, and of Raman scattering, a century later, vibrational spectroscopy has become one of the key techniques to characterize the structure of matter at the molecular scale. Indeed, vibrational transitions depend on the chemical composition and bonding arrangement of materials, therefore vibrational spectra can be can be considered as a material's molecular "fingerprint".

IR and Raman techniques are highly complementary since both result from transitions between quantized vibrational energy states but have different selection rules. Indeed, a given normal vibration may appear in the IR spectrum if at least one component of the electric dipole moment of the molecule changes during this vibration, while it may appear in the Raman spectrum if at least one component of the polarizability tensor changes during this vibration.

In this chapter we will describe for both spectroscopies the basic concepts, the experimental setups and the sample preparation procedures, discussing also metrological aspects. Selected examples of characterization of oxide nanoparticles will be discussed to highlight the potential and limitations of IR and Raman techniques.

4.6.2 Infrared spectroscopy

4.6.2.1 Basics and scope of the technique

Vibrational spectra were initially studied by passing infrared radiation through a sample and determining which was the fraction of the incident radiation absorbed at a particular energy. The IR region was the first non-visible region of the electromagnetic spectrum to be discovered since it was studied by the astronomer Sir William Herschel already at the beginning of the XIX century. Infrared spectrometers have been commercially available since the 1940s, based on dispersive elements. A great improvement occurred in the 1960s with the introduction of Fourier-transform spectrometers. Fourier-transform infrared (FT-IR) spectroscopy has drastically improved the quality of infrared spectra and minimized the acquisition time.

Since vibrational spectra are sensitive to the chemical composition and bonding arrangement, FT-IR spectroscopy is extremely useful in the study of nanoparticles (NPs). Indeed, NPs may be analyzed in a rapid and non-destructive way considering their intrinsic

IR bulk modes, shedding light into the structure of different kind of nanostructures, including hybrid and core-shell NPs [1]. The technique is also often employed to study the vibrations of functional groups present on the surface [2]. Moreover, IR spectroscopy of adsorbed probe molecules is a powerful investigation tool which allows obtaining information with "molecular resolution" of the nature, oxidation state and local structure of the surface sites of the NPs [3-6]. In particular, the surface centers, having a lower coordination than the bulk ones, are available for the interaction with probe molecules: as consequence of adsorption, the spectral features of probe molecules change, indirectly providing information on surface sites.

Different acquisition approaches can be adopted for FT-IR spectroscopy, including transmission, diffuse-reflectance (DRIFTS) and attenuated total reflection (ATR) [7]. ATR employs the evanescent wave formed at the interface between an internal reflection element (IRE) and the sample. The material of the IRE determines the range of applicable temperature, pressure and pH. The penetration depth into the material (in general few micrometers) depends on the angle of incidence, the wavelength and the indices of refraction of the sample and of the IRE [8].

Coupling an IR spectrometer to an optical microscope opens the possibility to investigate samples with a spatial resolution limited only by the diffraction limit of IR light (2.5 – 10 μm). This approach does not allow studying single NPs but is suitable to characterize small NPs assemblies [9].

In the following sections the sample preparation procedure for the different acquisition approaches and two selected case studies concerning the characterization of TiO_2 NPs will be discussed to highlight the potential of IR spectroscopy to investigate the nature of surface sites and the functional groups present at the NP surface.

4.6.2.2 Instrument set-up and sample preparation

A common FT-IR spectrometer consists of a source, interferometer, sample compartment, detector, amplifier, analog-to-digital converter, and a computer, as schematized in Figure 1. The source generates radiation which, after passing in the interferometer, goes through the sample and reaches the detector. After amplification and analog-to-digital conversion, the signal is transferred to a computer, which performs the Fourier transform.

FT-IR spectrometers are highly accurate and reliable measurement tools. The wavenumber scale of an interferometer is derived from the interference pattern of a helium–neon laser that acts as an internal reference for each scan. Since the wavenumber of this laser is known very accurately and is very stable, the wavenumber accuracy and repeatability for FT-IR spectrometers is better than for dispersive instruments (the so-called Connes advantage) [10]. Polystyrene reference materials are commonly employed to test the FT-IR spectrometer calibration.

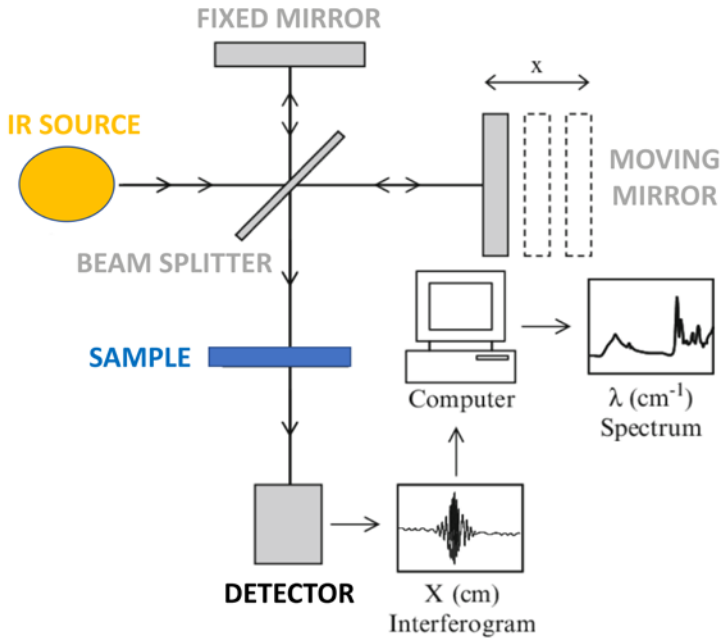

Figure 1. Schematic diagram of a FT-IR spectrometer for measurements in transmission mode.

The sample preparation is rather simple for DRIFTS, where the NPs powder is loosely placed in the sample cup, and for ATR, where the NPs are deposited on the IRE as a thin film. Conversely, to perform IR measurements in transmission NPs samples must be pressed in self-supporting pellets using a hydraulic press with a pressure of *ca.* 10 bar and inserted in gold frames to hold the pellets. To study the bulk vibrational modes, the sample can be diluted in a IR-transparent powder (often KBr). However, if the experiments involve the use of probe molecules, pure thin self-supporting pellets must be employed. In this case

pellets must have a mass thickness in the 10-15 $mg \cdot cm^{-2}$ range. Mass thickness, also known as mass deposition or mass coating, is the mass of an ideal pellet with basal surfaces each of 1 cm^2.

The investigation of probe molecules adsorbed on a NP surface with transmission mode IR spectroscopy requires working in controlled atmosphere. Therefore, the pellets are placed in cells equipped with IR-transparent windows (*e.g.* KBr or CaF_2), which can be connected to a conventional vacuum line (residual pressure < 10^{-4} mbar) allowing thermal treatments and adsorption-desorption experiments to be carried out *in situ* [11].

4.6.2.3 Case study: surface hydration and hydroxylation of NPs by IR spectroscopy

Understanding water/solid interactions is crucial for several fundamental and technological processes employing NPs, such as photocatalysis, electrochemistry, biomaterials, heterogeneous catalysis and corrosion [2, 12, 13]. TiO_2 NPs, being widely employed in aqueous environment as photocatalyst for pollutants abatement and as biomaterial [14, 15], represent an ideal system to discuss the potential of IR spectroscopy to characterize the state of adsorbed water molecules and hydroxy groups on the NPs surface. The investigation of the IR features of surface OH on TiO_2 NPs has been the subject of many papers [16-20] and the study of the vibrational frequencies of intrinsic OH groups in combination with DFT calculations can provide information on the exposed TiO_2 surfaces [21, 22].

In order to properly study ν(OH) and $\delta(H_2O)$ vibrational features of adsorbed water molecules and hydroxyls, the background due to the scattering of the IR radiation by the TiO_2 pellet must be removed by subtracting the spectrum of a TiO_2 pellet exposed to 20 mbar D_2O and then outgassed at room temperature (RT) (see Figure 2) [19].

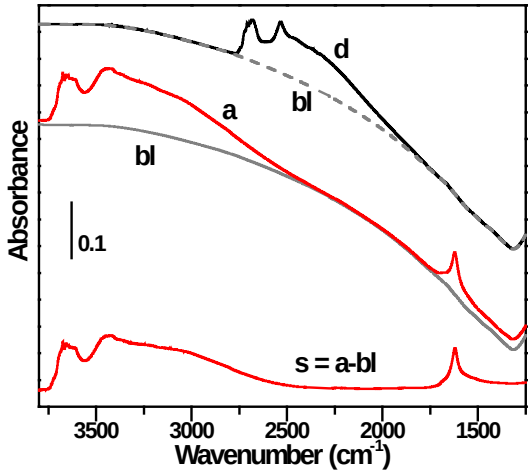

Figure 2. Removal of the contribution due to the scattering from IR spectra of TiO_2 NPs: a) spectrum of pristine TiO_2 NPs outgassed for 60 min at RT, d) spectrum of TiO_2 NPs outgassed at 873 K, exposed to 20 mbar D_2O and then outgassed at RT for 60 min; bl) spectrum after removal of the ν(OD) pattern in the 2750-1800 cm^{-1} wavenumber range from spectrum d delivering a reasonable baseline; s) "scattering corrected" spectrum of TiO_2 NPs outgassed for 60 min at RT resulting from the subtraction of simulated spectrum (bl) from spectrum (a). Unpublished Figure reporting data published in ref. [19].

After applying the scattering correction described in Figure 2, it is possible to study the evolution at increasing outgassing temperatures of the IR signals of OH groups and water molecules adsorbed on TiO_2 NPs. Figure 3 displays that is possible to properly isolate the signals due to hydroxyl groups with respect to the signals related to molecular water. In the spectra of the TiO_2 NPs sample outgassed at 373 and 473 K the water bending mode ($\delta(H_2O)$) is still clearly visible at 1620 cm^{-1}. In the sample outgassed at 573 K the intensity of the $\delta(H_2O)$ mode is diminished to only 1 % of the initial intensity in the sample outgassed at RT. Also the intensity of the broad absorption band due to the ν(OH) stretching mode of hydrogen bonded OH in the 3600-3000 cm^{-1} range is substantially reduced. In the 3750-3600 cm^{-1} range several signals related to isolated OH groups are present. In literature there is a general consensus about the assignment of the ν(OH) bands at frequencies higher than 3680 cm^{-1} to linear hydroxyls, while bands at lower frequencies are ascribed to bridged OH [19]. On the contrary, the specific attribution of the single components is still debated and several different interpretations have been proposed [16-22].

The detailed information about surface hydration and hydroxylation provided by IR spectroscopy is crucial to better rationalize the functional behavior of the NPs [23]. For

instance, it has been recently highlighted that the photodegradation kinetic of phenol on shape-engineered TiO_2 NPs strongly depends on the NP surface hydrophilicity [24].

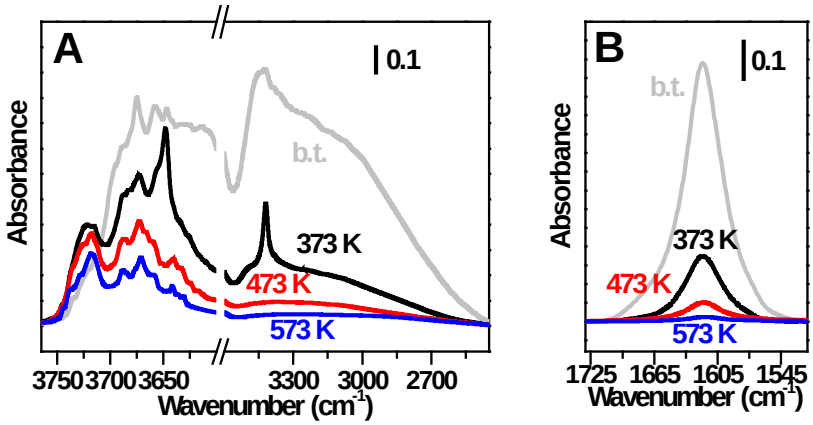

Figure 3. Scattering corrected (see Figure 2) IR spectra in the ν(OH) (panel A) and δ(H_2O) (panel B) regions of TiO_2 NPs outgassed for 60 min at RT, 373, 473 and 573 K. Unpublished Figure reporting data published in ref. [19].

4.6.2.4 Case study: investigation of surface Lewis acid sites and NP morphology by adsorbed probe molecules

The ideal probe molecule to investigate NP surface properties should be small (to avoid steric hindrance during adsorption), with spectral features sensitive to the nature of the surface centers, and should not significantly modify the NP surface upon adsorption. Possessing all these features, carbon monoxide is one of the most frequently employed molecules to probe the Lewis acid sites on different kind of NPs, including TiO_2, MgO, ZnO, SiO_2, ZrO_2, CeO_2, Al_2O_3 and metal NPs [4-6, 25, 26].

When CO is adsorbed on the surface cationic centers, its frontier orbitals are perturbed and three different kinds of interaction can be observed [4, 5]:

(i) electrostatic, due to the interaction between the electrostatic field of the surface cation and the CO charge distribution without electron transfer. It causes an increase of the CO stretching frequency (ν(CO)) with respect to that of CO in the gas phase at 2143.16 cm^{-1};

(ii) π bond, where the electronic density of *d* orbitals of the cation is added to the LUMO of CO: the ν(CO) of adsorbed molecules decreases with respect to the CO gas owing to the weakening of the C-O bond;

(iii) σ bond, where electronic density is transferred by metal ions with empty *d* orbitals to the HOMO of CO. Since the HOMO has a slightly anti-bonding character, the interaction causes a stabilization of the CO molecule, thus strengthening the carbon-oxygen bond and resulting in an increase of the CO stretching frequency.

As a case study, we discuss the adsorption of CO on TiO_2 NPs. The pellets TiO_2 must be outgassed at high temperature (873 K for 60 minutes in this experiment) to remove water and other adsorbed molecules from the NP surface before CO adsorption. The pellets are then oxidized with 10 mbar of O_2 for 30 minutes at 873 K, cooled down to 423 K in O_2 atmosphere and further cooled down to room temperature under outgassing. The treatment with O_2 is performed to remove the residual organic contaminants and to ensure the full stoichiometry of the oxide.

After this activation procedure, special care must be taken to avoid re-adsorption of molecular water by handling the sample in a cell with controlled atmosphere. The presence of water contaminations can be monitored by the rise of the signal related to the $\delta(H_2O)$ mode around 1620 cm^{-1}. After checking the absence of surface contaminations, CO is adsorbed at 40 mbar at RT and the sample is cooled down to 100 K. The progressive CO desorption should be performed at 100 K in order to gradually decrease the surface coverage till complete CO outgassing.

In the IR spectra, obtained for the adsorption of CO at 100 K on two different TiO_2 samples (Figure 4), several signals can be observed, and most of these spectral features are related to the internal stretching mode of CO interacting with the Ti^{4+} surface sites. Since their electronic configuration is d^0, only the electrostatic interaction and the σ bond formation with adsorbed CO is possible [27]. Therefore, its stretching frequency is directly linked to the electrophilicity, and thus to the Lewis acidity, of the surface Ti^{4+} centres located on extended surfaces, edges, steps and corners (in general there is a direct proportionality between shift of the ν(CO) and Lewis acidity) [28-30]. Moreover, since the stretching frequency of adsorbed CO is also strongly influenced by the lateral interactions occurring in the adlayers, it can give indirect information on the bidimensional packing of Lewis centres and hence of the structure of the different adsorbing faces. Therefore CO is not only an excellent probe of the individual sites, but can also give information about crystal

facets exposed to CO and hence particles morphology when the interpretation of the IR spectra is supported by DFT calculations [11, 20, 31-35].

Figure 4A shows the HR-TEM images of two different kinds of TiO_2 nanoparticles: shape-engineered TiO_2 NPs with a well-defined bipyramidal shape and commercial Evonik TiO_2 P25 NPs with complex morphology [11, 24]. On the basis of a comprehensive set of periodic DFT calculations and experimental data thoroughly discussed in literature [11, 20 , 24, 31, 32, 34, 35], it is possible to correlate the different CO absorption bands to different TiO_2 surface structures (Figure 4B):

- the weak feature at 2212 cm^{-1} is due to a combination mode among the internal CO stretching mode responsible of the main peak and a frustrated translational CO mode;
- the signal at 2206 cm^{-1} is due to CO adsorbed on low coordinated Ti sites, which are usually denoted in literature as α sites;
- the shoulder at 2184 cm^{-1} is ascribed to CO interacting with the {110} anatase surfaces;
- the main peak at 2179/2178 cm^{-1} is due to CO adsorbed on the {101} TiO_2 anatase surfaces. The actual position can differ of 1/2 cm^{-1} depending on the extension of the coupling among adsorbed CO molecules. The lower the value, the higher the extension of highly regular (e.g steps and kinks free) portions of {101} surfaces.
- the band at 2164 cm^{-1} is related to the {100} TiO_2 anatase surface;
- the signal at 2158 cm^{-1} is ascribed to CO interacting with few residual OH groups;
- the weak component at 2149 cm^{-1} is due to CO adsorbed on the TiO_2 rutile phase;
- the band at 2139 cm^{-1} is due to physically adsorbed CO forming a surface multilayer;
- the signal at 2127 cm^{-1} is related to ^{13}CO adsorbed on the {101 TiO_2 anatase surfaces.

The IR spectra of the two kinds of TiO_2 nanoparticles are both dominated by the signal of CO adsorbed on the {101} TiO_2 anatase surfaces. However, the spectrum of TiO_2 P25 nanoparticles show a significant population of Ti^{4+} sites in low coordination at minority

surfaces (e.g. {110}), steps and edges: this observation can contribute to explain the differences in photocatalytic activity of the two samples [11].

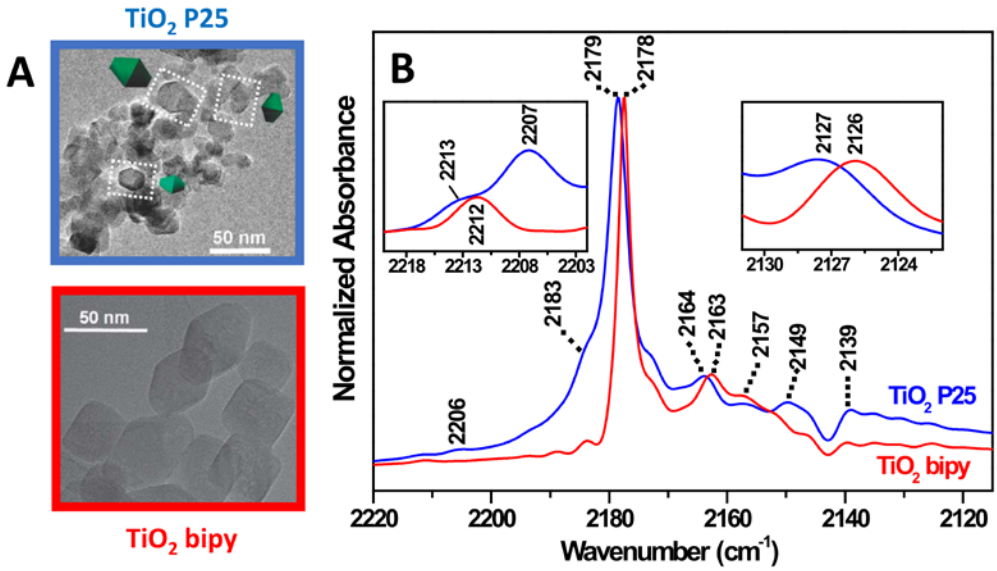

Figure 4. (A) HR-TEM images of Evonik TiO_2 P25 and TiO_2 bipyramidal NPs. (B) IR spectra of CO adsorbed at *ca.* 100 K on TiO_2 P25 and TiO_2 bipyramidal NPs. The samples were outgassed for 60 minutes at 873 K before CO adsorption. See the text for the assignment of the different spectral components. Unpublished Figure reporting data published in ref. [11].

4.6.3 Raman spectroscopy

4.6.3.1 Basics and scope of the method

Raman spectroscopy is a vibrational optical spectroscopic technique based on the inelastic scattering of light by matter. This phenomenon was postulated theoretically in 1923 by Smekal [36]. In 1928 the first experimental observation of Raman scattering effect was reported by two Indian physicists, Raman and Krishnan [37] and independently by Mandelstan and Landsberg in the Soviet Union [38]. Raman spectroscopy is a fingerprint technique that allows to identify molecules with high specificity and to identify and quantify analytes with minimum requirements for sample treatment. However, since Raman scattering is intrinsically almost always weak, the acquisition of “normal” Raman spectra of low concentration analytes becomes quite difficult. Typically, total Raman

scattering cross-sections are about 10^{-29} cm^2 per molecule, whereas typical cross-section for fluorescence emission, ultraviolet and infrared absorption are about 10^{-16}, 10^{-18} and 10^{-21} cm^2 per molecule, respectively [39]. This accounts for the slow growth that elapsed from the discover of the Raman method which was pushed by the emergence of powerful light sources like lasers. Starting around the 1980s the advances on the development of compact lasers, detectors and optical filters, allowed lower costs integrated instruments to be produced commercially. As a consequence, Raman spectroscopy has been adopted as a routinely method in many fields because simple and fast.

One of the main advantages of the technique is that sample preparation is non-destructive and it does not require previous treatments or the use of labelling agents. Basically any type of material or mixture can be probed as long as it is characterized by Raman active vibrational modes. Accordingly, Raman spectroscopy is an extremely versatile technique for chemical characterizations. Furthermore, the recent development of portable Raman spectrometers for quick in situ analysis allows minimizing the issues related to sample transportation and manipulation. This kind of equipment is necessary, for example, for the non-destructive investigation of unmovable artistic objects or in case of organic or biological samples whose features may alter during handling, such as perishable food [40].

Whereas already assessed as effective technique for qualitative analysis, Raman spectroscopy does not provide a powerful method for the quantitative determination of substances: different authors exploit different approaches to obtain the value of solute concentration in solutions, but results are often inconsistent. The issue is that Raman intensity depends not only on the analyte concentration, but also on the intensity of the incident light, namely on the measurement conditions such as the power of the excitation source, the instrumental optical configuration and sample alignment. Here comes the need for the calculation of the intensity ratio between the analyte signal and a reference band, which implies the rise of problems related to the employment of an external or internal standard [41].

However, even qualitative analyses are subject to considerable limits. The main issue concerns the low Raman scattering cross-sections (10^{-29} cm^2). The consequence is a very weak scattering signal, which limits Raman sensitivity and requires long exposure time or high-power lasers. This prevents its employment as high-resolution technique since it

would imply a low limit of detectability of the order of few molecules [42]. The need for a technique sensitive enough for traces or even single molecule detection interests a variety of research fields, spanning from biology, where up to now single-molecule detection relies on the attachment of fluorescent markers, to analytical chemistry, from forensic science to the study of artistic objects, to semiconductors industry, where there is large demand for characterization on the nanoscale level [43].

Moreover, Raman signal weakness causes it to be often overwhelmed by the protruding background of fluorescence occurring as an alternative mechanism for electrons return to the ground state after excitation through visible light. This effect is particularly probable in case resonance Raman spectroscopy is performed [44].

In conclusion, the suitability of such a powerful technique like Raman spectroscopy is heavily straitened by limitations in resolution and sensitivity. However, the chance of exploiting the advances in the nano-technology field led to the birth of advanced Raman spectroscopies like Surface-Enhanced Raman Spectroscopy (SERS), Surface-Enhanced Resonance Raman Spectroscopy (SERRS) and Tip-Enhanced Raman Spectroscopy (TERS), whose main merits are intensity and resolution improvements.

4.6.3.2 Raman microscopy setup

Typically, Raman instruments consist of an optical microscope combined with a laser source, a motorized stage, a dispersive grating and a CCD detector, as schematized in Figure 5. This configuration allows to magnify a selected region and collect spectra on a micrometric scale.

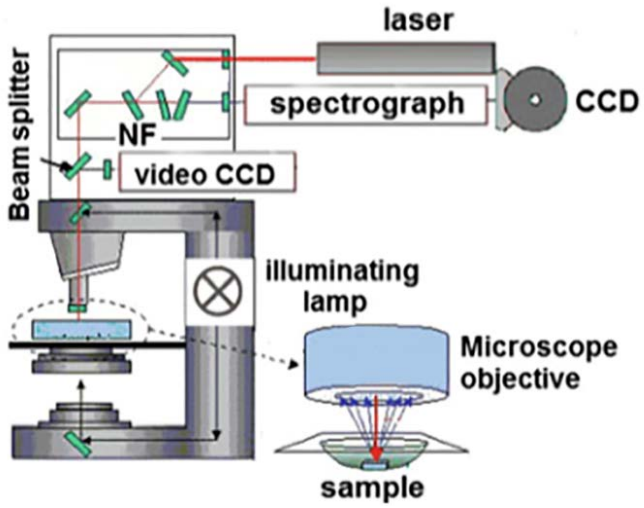

Figure 5. Schematic diagram of an experimental set-up of a μ-Raman spectrophotometer.

To maximize the Raman signal, every part of the system must be optimized for the highest transmission, throughput, and efficiency. It is very easy to lose sensitivity if the components are not properly chosen.

The laser beam has to pass into the microscope twice through a dichroic or holographic beam splitter. The reflectivity of the beam splitter should be as high as possible at the laser excitation wavelength, and its transmission for the Raman light should be high as well. Dichroic filters available todays can ensure reflectivity up to 95% at the laser wavelength and, at the same time, transmission of about 98% for the Stokes-shifted Raman light.

For efficient suppression of the Rayleigh line, an edge or notch filter having a throughput of >95% for the Stokes-shifted Raman lines must be used. Most commercially available spectrometers have a throughput (including gratings) of only 30–35% (at 532 nm), although the gratings have an efficiency of up to 80%. This means that more than 50% of the light is lost because of the coatings of the spectrometer mirrors.

Continuous lasers are generally used in dispersive Raman spectroscopy and the choice of excitation wavelength depends on sample characteristics whether it is in liquid or solid state, and in the latter case of on its structure (e.g. if it is bulky or composed of micro- or nano-crystallites). Taking into account that Raman intensity is proportional to ω_{inc}^{4} where is laser light frequency. This means that, in the visible range, excitation at 400 nm leads to Raman signals one order of magnitude larger than excitation at 800 nm.

Furthermore, the shorter is the excitation wavelength the lower is the lateral resolution which, in the *xy* plane (r_{xy}) is defined by the Ralyleigh limit:

$$r_{xy} = \frac{0{,}61\lambda}{NA} \qquad \text{(Eq. 1.1)}$$

where λ is the wavelength of the excitation radiation and NA the numerical aperture of the objective lens. A better value of lateral resolution can be obtained using objective lens with higher NA and/or a shorter wavelength of the exciting radiation. In this respect it is worth to mention that unfortunately the samples often show strong fluorescence when excited in the UV or blue region of the visible spectrum. Therefore, to reduce the fluorescence contribution, they need to be analyzed with less energetic radiation, like in the red or near infrared region.

The Raman intensity also depends on the laser power, which deserves to be chosen carefully to avoid beam damage by heating up the sample. Sample heating is a common problem associated with Raman spectroscopy because the samples unavoidably absorb at least a part of the incident radiation. In general, the rise in temperature depends on the thermal conductivity and optical properties of the sample on the one hand side and on the laser power and wavelength on the other. Thermal or photo degradation is often an issue for organic molecules, dyes, metallic complexes, polymers or biological samples.

In particular nanoparticles and other nanostructured samples show thermal properties different from that of bulk materials. It has been demonstrated that at a laser power of a few mW focused on nanostructures the melting point can easily reached [45]. Taking into account laser beam damage, typically a laser power in the range from a few µW to several hundreds of mW is used in Raman spectroscopy. The selection depends also on the used wavelength of the laser light.

The grating in a Raman spectrometer disperses the “white” light signal of the sample onto the CCD detector by deflecting each wavelength at a slightly different angle. The number of grooves per millimeter forming the grating determines its dispersion characteristics. A high number of grooves/mm (lines/mm) results in a high dispersion meaning a high spectral resolution. However, because a CCD detector has a limited number of pixels the spectral range covered becomes smaller when the spectral resolution is increased.

For imaging Raman analysis an effective coupling of an optical microscope to a Raman spectrometer requires a spatial filter for controlled spatial information along the XY (lateral) and Z (depth) axes.

The calibration should encompass both the spectral features providing chemical information, and the quantitative aspect of the measurement. As far as the former are concerned, a variety of valid calibration procedures have already been developed and must applied for regular calibration of the Raman spectrophotometers. Conversely, a quantitative sample analysis in terms of either the amount of analyte or its spatial distribution requires, besides signal intensities, the accurate determination of the confocal volume and of lateral and in-depth resolutions. These characterize the confocal optical microscope integrated in the spectrophotometer and, unfortunately, they still lack of standards for precise calibration. This is a recent challenge in the related metrological research activities.

The determination of the confocal volume is still a debated topic and the methods used for its estimation as provided in literature do not satisfy the requirements to become standards so far. The confocal volume can be approximated to be an ellipsoid along the radial direction on the focal plane. The illumination intensity decreases following approximately a Gaussian trend, thus outlining the spot size and defining the lateral resolution achieved. Few procedures have already been proposed and generally accepted for the estimation of the horizontal field of view. Conversely, particular concern is still devoted to the definition of the volume height. The experimental methods developed for the measurement of the ellipsoid vertical axis are usually based on depth profiling of heterogeneously layered samples and on the detection of the respective Raman intensities as function of vertical position. The main issue lies in the mismatch between refraction indices in correspondence to the interfaces, which causes changes in the beam dispersion angle as the beam crosses the sample. As a consequence, the positioning of interfaces within the sample thickness obtained through confocal Raman measurements loses accuracy: surface layers appear thinner than they actually are and the interfaces much broader. Figure 6 depicts the effect of refraction on depth resolution, which appears to increase at deeper positions. This explains the different thickness values obtained for buried substructures of the same thickness at different depths. Such effects hinder the exploitation of experimental methods

based on depth profiling for the accurate determination of Raman confocal volume vertical size and, consequently, of depth resolution [46-48].

Together with depth profiling, Raman spectroscopies are commonly exploited for analytes imaging: as the laser scans the specimen, 2D maps can be obtained at different focal planes and then possibly assembled in a 3D replication of the sample volume, which conjugates chemical and dimensional information. The lateral spatial resolution is known to be subject to Rayleigh diffraction limit, which depends on the excitation wavelength and the objective employed. Common values vary around 1 μm, but they can be lowered by the presence of confocal pinholes or slits.

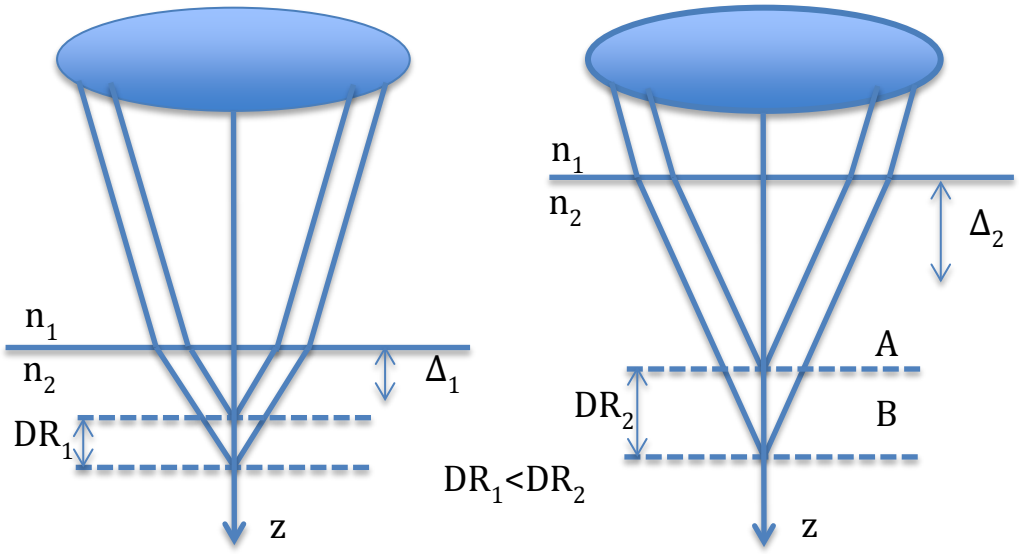

Figure 6. Schemes showing the effect of refraction of the beam light coming from the objective lens (hemisphere), due to a difference in refraction indices $n_1 \neq n_2$. If the two refractive indices are equal, all rays would be focused at the same nominal depth Δ. Instead, the marginal rays are actually focussed at deeper positions (B) than the paraxial ones (A). As a consequence, the depth resolution (DR) is refraction-limited and it worsens as the focal plane moves deeper inside the sample [46].

A standard specimen for the spatial calibration of Raman microscopes has been developed in the Physikalisch-Technische Bundesanstalt (PTB) [49], the National Metrology Institute of Germany. It is a silicon chip, some of whose areas have been covered with a thin Au/Pd layer. The latter are distinguished on the basis of Si Raman signal intensity, which results attenuated with respect to the peak detected in correspondence of Au/Pd-free zones. These

are patterned with point, line and two-dimensional checkboard-like structures, variously displaced on the chip surface and differently sized within few micrometres range. The corresponding distribution of chemical composition obtained by Raman mapping provides the calibration of the instrument component assigned to x-y positioning and the microscope's optical resolution. In order to ensure the traceability to the SI meter standard, the chip dimensions are assessed by means of a calibrated Scanning Force Microscope.

4.6.3.3 Instrument calibration

Raman spectroscopy requires a careful calibration of the wavelength and intensity scales. For absolute wavelength calibration the emission lines of a neon lamp are often used as a reference. As a typical procedure, the Neon spectrum resulting from the calibration measurement is used to correlate the pixel positions on the CCD chip with the wavelengths in the reference spectrum. Values of pixel position are plotted against the known reference Neon peak wavelengths [50] and the data fitted with a cubic polynomial function in order to get the calibration function that allow to obtain the correlation between peak intensity and the wavelength on the entire spectrum.

Later the Raman shift frequency at each CCD pixel is obtained by converting the wavelengths corresponding to each pixel to a frequency with subsequent subtraction of the laser excitation frequency [50]. Alternatively, different solids and liquids can be chosen as Raman shift standards instead of the neon lamp emission, supposed that they present numerous Raman bands to allow calibration in a wide spectral region. For that purpose eight materials are readily available from commercial sources at high purity, *i.e.*: polystyrene, cyclohexane, naphthalene, 4-acetamidophenole, acetonitrile-toluene 50:50, 1,4-bis(2-methylstyryl)benzene, sulfur and benzonitrile [51].

The intensity scale of the Raman spectrometer is calibrated using a broadband light source of known spectral irradiance resulting in the spectral intensity-response correction that characterizes the Raman system. The reference material used is a standard commercialized by NIST (National Institute of Standard Technology, USA), SRM 2241®, which consists of an optical glass that emits a broadband luminescence spectrum when irradiated with a laser of proper wavelength. The shape of the luminescence spectrum of the glass is described by a mathematical expression that gives the relative spectral intensity *vs* the

wavenumber (cm^{-1}) expressed as the Raman shift from the excitation laser wavelength [52].This model function for a calibration, together with a measurement of the luminescence spectrum of SRM 2241®, has to be used to determine the spectral intensity-response correction that characterizes the Raman instrument.

The luminescence spectrum of SRM 2241® is described by a fifth order polynomial function of the type:

$$I_{SRM}(\Delta\nu) = A_0 \times A_1(\Delta\nu)^1 \times A_2(\Delta\nu)^2 \times A_3(\Delta\nu)^3 \times A_4(\Delta\nu)^4 \times A_5(\Delta\nu)^5 \text{ . (Eq. 2)}$$

$I_{SRM}(\Delta\nu)$ is the reference spectral intensity of the standard reference material; $\Delta\nu$ is the wave number in units of Raman shift. The polynomial coefficients, A_n, are specific for SRM 2241® material. The normalized spectrum of SRM 2241®, for 785 nm laser excitation is reported in literature [52].

The intensity correction of a generic Raman spectrum of a sample, collected with a well defined data point spacing in the Raman shift (cm^{-1}), is done by first calculating the spectral intensity correction, $C_{SRM}(\Delta\nu)$, using the reference spectral intensity of the standard reference material $I_{SRM}(\Delta\nu)$ and the actual luminescence spectrum collected on the standard, $S_{SRM}(\Delta\nu)$, by the following equation:

$$C_{SRM}(\Delta\nu) = I_{SRM}(\Delta\nu)/S_{SRM}(\Delta\nu) \text{ (Eq. 3)}$$

Then the corrected spectrum, $S_{CORR}(\Delta\nu)$, is calculated by multiplication the $C_{SRM}(\Delta\nu)$ with the sample spectrum, $S_{MEAS}(\Delta\nu)$:

$$S_{CORR}(\Delta\nu) = C_{SRM}(\Delta\nu) \times S_{MEAS}(\Delta\nu) \text{ (Eq. 4)}$$

The calibration model certified by the value of the polynomial coefficients is valid for Raman shifts in the range between 200 cm^{-1} and 3500 cm^{-1} for a temperature range of 20 °C to 25 °C.

4.6.3.4 Nanoparticle preparation for Raman analysis

For an analysis of nanoparticles deposited on a sample holder from a suspension a certain level of homogeneity in terms of their distribution at the micro- and nano-scale has to be achieved in that suspension, and maintained during the deposition of a film consisting of

non-aggregated NPs. This can be a challenge because several chemical and physical reasons that depend on the nature of the nanoparticles, their shape and dimension and the medium in which the nanoparticles are suspended play a role. In a suspension nanoparticles tend to migrate and stick together forming agglomerates due to strong inter-particle interaction.

Theory papers address this issue of a quantitative evaluation of the dispersion [53]. Many tools are available for sample preparation and recipes have been proposed to establish and control the aggregation of nanoparticles in suspension[54].

From an experimental point of view for measurement using a Raman microscope we suggest using a few simple steps that help to obtain suspension of nanoparticles with a minimized probability of their undesired aggregation.

When preparing a well-suited NP suspension for characterization by Raman microscoy it is important to have sufficient knowledge of the basic chemical properties of the NPs character to select an appropriate solvent and, eventually, dispersing agents. Therefore, the powders are at first categorized to be hydrophobic or hydrophilic by measuring their contact angle (CA) with de-ionized water (DI H_2O).

As described in Figure 7, NPs received in powder form are then dispersed in the solvent in an ultrasonic bath at controlled temperature to destroy any aggregates. The uniformity of the dispersion strived for is controlled by dynamic light scattering analysis (DLS) that provides the hydrodynamic radius of the objects in solution. The solvent is then evaporated in controlled atmosphere to achieve a dried layer of NPs for Raman microscopic analysis, Although some re-aggregation during drying occurs, the spatial distribution of NPs in the dried film reflects the suspension homogeneity.

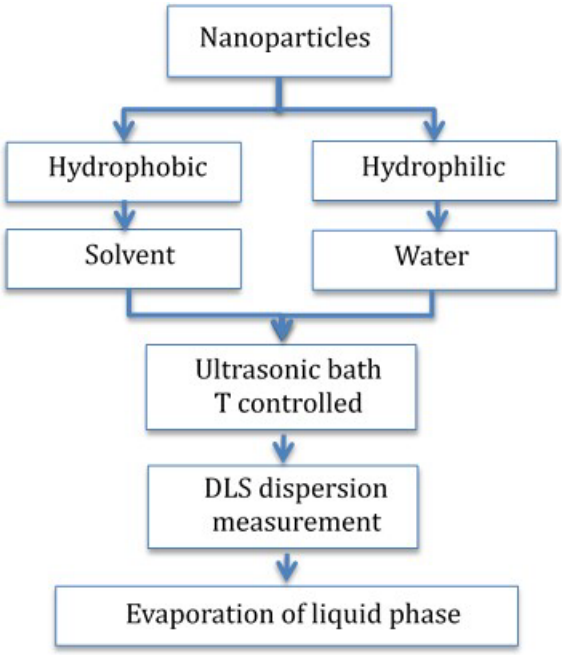

Figure 7. Procedure for preparation of nanoparticles received as powder for Raman analysis.

4.6.3.5 Case study: Quantification of TiO_2 NPs phase composition by Raman spectroscopy assisted by chemometrics

TiO_2 occurs in nature as three main different polymorphs, which show different chemical-physical properties: rutile (tetragonal), anatase (tetragonal) and brookite (orthorhombic).

When dealing with TiO_2 nanoparticle mixtures it is often important to precisely quantify the amount of these three different phases. In the following we describe a chemometric calibration and validation protocol of analysis devoted to classify and quantify different phases in TiO_2 NPs binary mixtures by Raman spectroscopy.

Owing to the different spatial arrangement of Ti and O atoms into the elementary crystal cell, anatase, rutile and brookite, are characterized by different vibrational modes and provide significantly different Raman spectra, see Figure 8 [55-57].

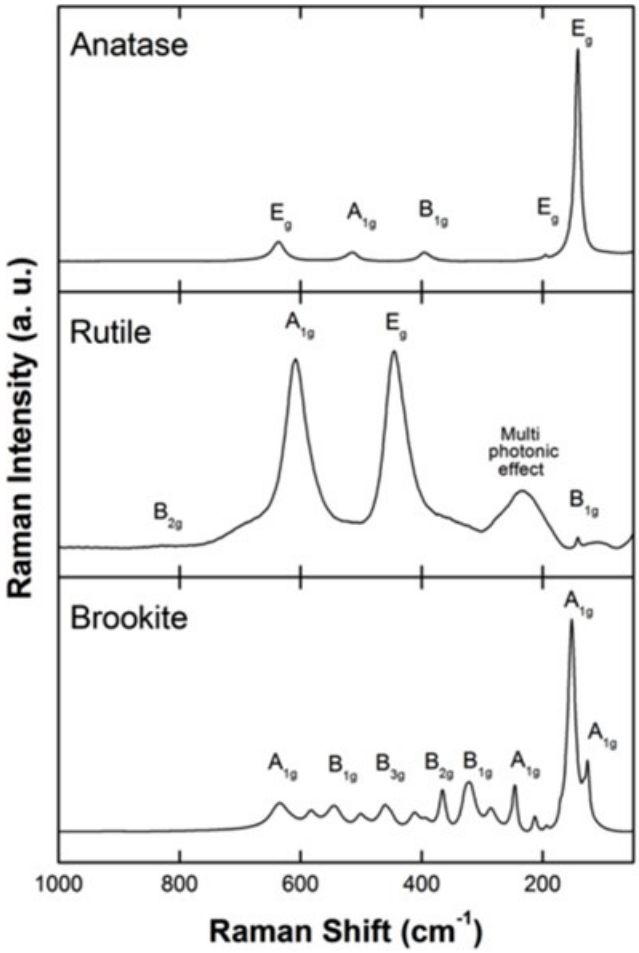

Figure 8. Anatase, rutile and brookite Raman spectra with vibrational mode assignment

Raman scattering of rutile involves four Raman active vibrations [57]: (A_{1g}) 143 cm^{-1}; (E_g) 447 cm^{-1}; (A_{1g}) 612 cm^{-1}; (B_{2g}) 826 cm^{-1}. Anatase has six active vibrations modes [55]: (E_g) 144, 197, 640 cm^{-1}; (B_{1g}) 400, 519 cm^{-1}; (A_{1g}) 507 cm^{-1}. While Raman active modes of brookite are seventeen [56]: (A_{1g}) 127, 154, 194, 247, 412, 640 cm^{-1}; (B_{1g}) 133, 159, 215, 320, 415, 502 cm^{-1}; (B_{2g}) 366, 395, 463, 584 cm^{-1}; (B_{3g}) 452 cm^{-1}.

Nano powders of anatase, brookite and rutile were synthesized by the hydrothermal route. Anatase and brookite were prepared starting from the same precursor, the titanatrane (i.e. Ti(triethanoleamine)). Reactions have been conducted in a stainless-steel high-pressure reactor. Pure anatase samples were prepared by adjusting the pH of the solution with NaOH up to a final pH=11 value. The vessel temperature was set at 220 °C. By adjusting the pH of the precursor solution at 12.5 and the temperature at 180 °C a pure brookite suspension was obtained. Rutile was prepared from $TiCl_4$ in HCl 2 M at a temperature of 180°C.

After the synthesis, the so obtained nano powder suspension were purified following a procedure involving multiple steps of centrifugation and re-suspension in ultrapure water, UV-light treatment in presence of H_2O_2, dialysis, and freeze drying.

A complete and stable de-agglomeration of the powder mixtures was obtained by suspending the TiO_2 nano powders in volatile organic solvent and then placing the mixture in an ultra-sound bath in water equipped with temperature control. Reference samples were prepared by dispersing in spectroscopic grade acetone (purity > 99.9%, non-volatile residue 0.0003%) carefully weighted amounts of different TiO_2 phases. Fraction percentage by weight (X_a) for the *a* component in a generic *a*-*b* mixture was calculated as follows:

$$X_a = \frac{x_a}{x_a + x_b} \cdot 100$$

where x_a and x_b are the weight of *a* and *b* components respectively.

The suspensions were then homogenized for 10 minutes in ultra-sonic bath at 15 °C and at a power of 80 W. Then, the suspensions were completely dried in air trying to obtain homogenous films.

Raman measurements were conducted with a Thermo Scientific DXR™ Raman dispersive instrument endowed with a motorized stage with micrometric resolution and a camera for the micro mapping of the sample. Measurements were performed using an excitation laser wavelength of 532 nm, a laser power of 1 mW, and an objective lens of 20x long working distance was used. Maps were collected in a 400 μm^2 area using a step size of 2 μm. The spectral range between 300 cm^{-1} and 800 cm^{-1} resulted to be the most interesting for the application. The choice of Raman mapping strategy, instead of single point spectra, was taken because single points spectra could not be representative of the entire sample, due to the limited area of the sample analyzed by a single point acquisition (approximately a 1.3 μm diameter corresponding to the laser spot-size). Indeed, it can be observed in Figure 9-b that by collecting a single spectrum in different locations, close regions of the same samples led to different ratios of peaks intensity, suggesting a locally different composition, even though the mixture was previously homogenized. This effect of agglomeration at the nanoscale is due to migration provoked by the differences in surface

energy between the NPs of different phases. To handle the problem of the micro-scale separation of particles, Raman maps composed of 25 pixels (yielding 25 Raman spectra) were collected in an area of 400 μm^2 (Figure 9a). Then the spectra were averaged for each map leading to one single spectrum taken to be representative for the entire area. Comparing the results of different maps collected on the same sample it can be observed that the average spectra are almost identical to each other, see Figure 9c. In this way it was confirmed that the mapping strategy is straightforward to handle the problem of local inhomogeneities. This approach was used to map samples prepared from mixtures of nanoparticles of different phase to obtain an average spectrum witch is representative for the sample. Such a spectrum contains weighted information from all the components in the mixed phase samples.

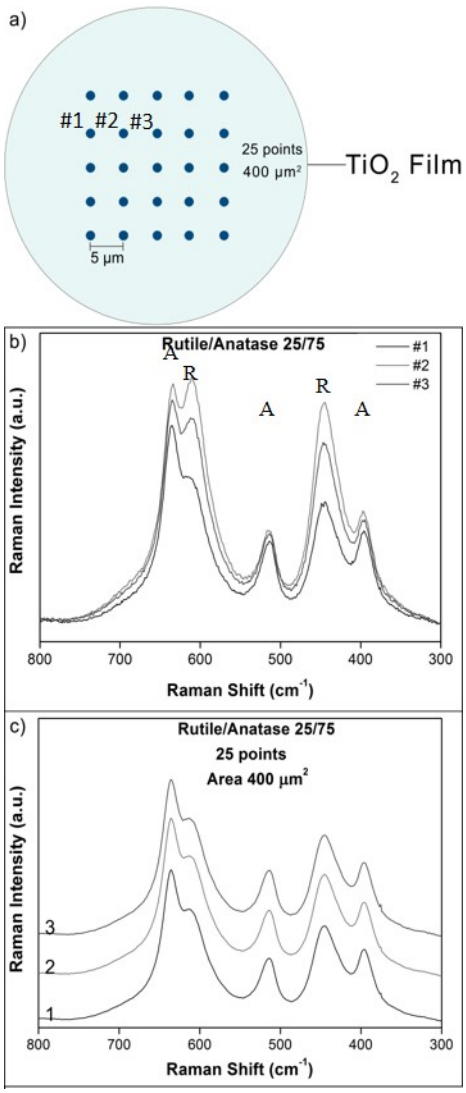

Figure 9. a) Scheme of the method using mapping of a sample which is here a spot of TiO_2 NP suspensions dried on a sample holder; b) Raman spectra of three close points with the number 1,2 and 3 in the legend, of a rutile-anatase 25/75 w/w mixture; 300-800 cm^{-1} spectral region. Anatase and rutile characteristic peaks are characterized by A and R labels, respectively; c) Averaged spectra of a rutile-anatase 25:75 w/w mixture. Each spectrum derives from 25 points maps on three different 400 μm^2 mapping areas.

Reference samples were prepared by dispersing weighted amounts of each two different TiO_2 phases in spectroscopic grade acetone. Raman measurements were performed using an excitation laser wavelength of 532 nm, a laser power of 1 mW, and an objective lens of 20x working distance. Maps were collected in a 400 μm^2 area using a step size of 2 µm. Raman maps were acquired to represent the overall sample by handling local composition inhomogeneities on the micro scale.

Raman spectroscopy coupled with chemometric analysis to maximize the extraction of useful information from the data sets, were used in order to recognize by Discriminant Analysis Classification [58], and quantify, using Partial Least Squares Regression [59], the amount of different TiO_2 phases in binary mixtures.

Classification methods are supervised chemometric techniques which allow to obtain a mathematical model able to assign each object to a proper class on the basis of a set of measurements used as training set. Among them, Linear Discriminant Analysis (LDA), starting from a calibration set, makes use of information on the classes as input. The method calculates a linear discriminant that separates classes in such a way that objects in the same class are more similar to each other with respect to those of other classes. This is done by identifying directions that minimize the variance within-class and maximize that between-classes.

The LDA input data set consists in a $n \times m$ matrix of *x* data and a response vector of dimension n, where n represents the number of samples (Raman spectra in this case) in the calibration set and m is the number of monitored variables. In this specific case, the m variables were the Raman shifts of spectra and the *x* data are the Raman intensities for each Raman shift.

The results of a classification analysis by LDA can be presented as a Cooman's plot in which the distances of each sample from the center of the different classes are plotted against each other in a scatter plot. In a Cooman's plot, the three axes represent the distance from the center of one class. As it is shown in the Cooman's plots in Figure 10, the classification model enables to separate pure phases from binary mixtures and to recognize what phases are present in the sample.

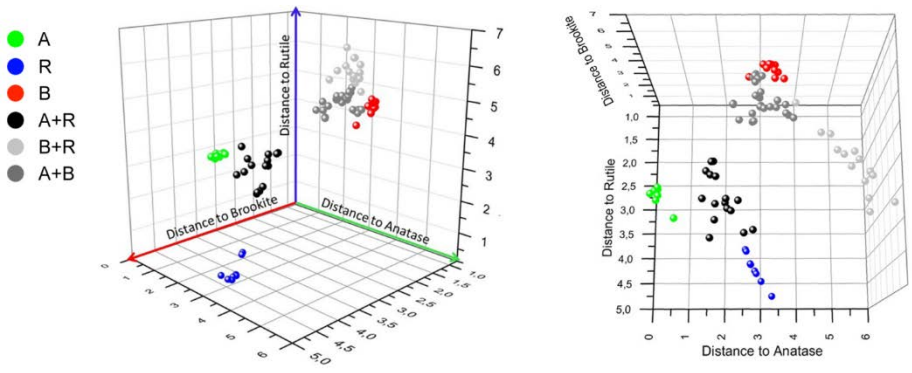

# of Samples	121
Non Error Rate	99.96%
Specificity	A-B 90% Others 100%
Sensitivity	B 90% Others 100%

Figure 10. Cooman's plot for the classification of 100% anatase, rutile, brookite and each 50% of anatase-brookite, anatase-rutile and rutile-brookite mixtures. To better resolve the separation, the Cooman's plot is shown using two different perspectives of view. A, B and R stay respectively for anatase, brookite and rutile, respectively.

After the classification of the mixtures by LDA, which allows to determine the components present in the sample, the second step of this work was the development of a chemometric model able to quantify the amount of each phase in a binary mixture sample. The calibration training set was built excluding pure phases, since they are accurately recognized by LDA and do not need quantification.

Partial Least Squares (PLS) was chosen as regression model to obtain a quantification method. PLS is one of the most common regression algorithms in the field of chemometrics in general, and spectroscopy in particular. In the typical approach, a training set of n samples is used. Each set is described by a set of m variables $x_i \ldots x_m$ - in our case intensities of Raman shifted signals of phase specific Raman active vibrations - and a response y_n - in our case the composition ratio of each sample - (where x_n and y_n are often referred to as inter-correlated variables). PLS first operates by looking for a linear relationship between objects (Raman Spectra) and response (composition) by maximizing the covariance between *x* data (the intensities) and responses. The PLS plots for the training sets of actual phase fraction vs calculated phase fraction for the three binary mixtures analysed are showed in Figure 11. The three quantification models had a linear regression coefficient (R^2) close to 99%.

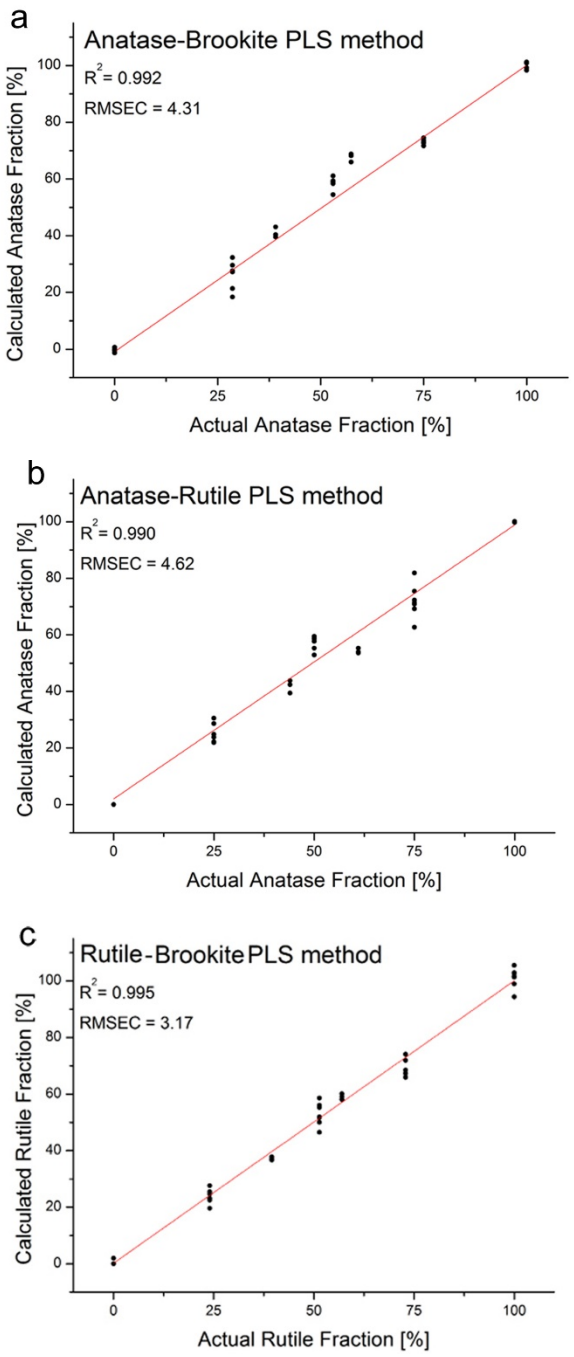

Figure 11. PLS Plot of actual vs calculated phase fraction for anatase-brookite mixtures (a), anatase-rutile mixtures (b) and rutile-brookite mixtures (c).

This Raman case study summarizes all the steps necessary to reach the goal of detection and quantification the nanomaterials in powder form using Raman spectroscopy.

Pure phases of TiO_2 in form of anatase, rutile and brookite were synthesized using a hydrothermal method in order to obtain chemically well-defined powders with high purity grade. Chemometric analysis and Raman spectroscopy were used in order to classify by Discriminant Analysis, and quantify, using Partial Least Squares, the phases' amount of different TiO_2 types in binary mixtures. Raman mappings were used in order to handle the micro-scaled inhomogeneity in samples.

Discriminant analysis was able to well separate the pure phases (anatase, rutile and brookite) from the mixtures (anatase-brookite, anatase-rutile and rutile-brookite). 93% of validation samples were assigned in the correct class and the model was able to distinguish mixture of 98% phase composition from pure phases with accuracy of 100 % for AR, and BR mixtures and of 0.9 for AB. Partial Least Squares was useful to quantify TiO_2 phases in mixtures. The validation was performed using external standards and the 87% of calculated compositions were statistically close to real values at confidence level of 95%.

4.6.4 References

[1] A.I. Lopez-Lorente, B. Mizaikoff, Recent advances on the characterization of nanoparticles using infrared spectroscopy Trac-Trends Anal. Chem. 84 (2016) 97-106.

[2] J.L. Skinner, P.A. Pieniazek, S.M. Gruenbaum, Vibrational Spectroscopy of Water at Interfaces Accounts Chem. Res. 45 (2012) 93-100.

[3] G. Busca, The surface acidity of solid oxides and its characterization by IR spectroscopic methods. An attempt at systematization Phys. Chem. Chem. Phys. 1 (1999) 723-736.

[4] K.I. Hadjiivanov, G.N. Vayssilov, Characterization of oxide surfaces and zeolites by carbon monoxide as an IR probe molecule in: B.C. Gates, H. Knozinger (Eds.), Advances in Catalysis, Vol 47, Elsevier Academic Press Inc, San Diego, 2002, pp. 307-511.

[5] C. Lamberti, A. Zecchina, E. Groppo, S. Bordiga, Probing the surfaces of heterogeneous catalysts by in situ IR spectroscopy Chem. Soc. Rev. 39 (2010) 4951-5001.

[6] Y.M. Wang, C. Woll, IR spectroscopic investigations of chemical and photochemical reactions on metal oxides: bridging the materials gap Chem. Soc. Rev. 46 (2017) 1875-1932.

[7] L. Mino, IR spectroscopy as a tool to investigate photocatalytic reactions at oxide surfaces Rend. Lincei.-Sci. Fis. Nat. 28 (2017) 143-149.

[8] B.L. Mojet, S.D. Ebbesen, L. Lefferts, Light at the interface: the potential of attenuated total reflection infrared spectroscopy for understanding heterogeneous catalysis in water Chem. Soc. Rev. 39 (2010) 4643-4655.

[9] M. Dendisova, A. Jenistova, A. Parchanska-Kokaislova, P. Matejka, V. Prokopec, M. Svecova, The use of infrared spectroscopic techniques to characterize nanomaterials and nanostructures: A review Anal. Chim. Acta 1031 (2018) 1-14.

[10] F. Zaera, New advances in the use of infrared absorption spectroscopy for the characterization of heterogeneous catalytic reactions Chem. Soc. Rev. 43 (2014) 7624-7663.
[11] C. Deiana, M. Minella, G. Tabacchi, V. Maurino, E. Fois, G. Martra, Shape-controlled TiO_2 nanoparticles and TiO_2 P25 interacting with CO and H_2O_2 molecular probes: a synergic approach for surface structure recognition and physico-chemical understanding Phys. Chem. Chem. Phys 15 (2013) 307-315.
[12] C. Sun, L.-M. Liu, A. Selloni, G.Q. Lu, S.C. Smith, Titania-water interactions: a review of theoretical studies J. Mater. Chem. 20 (2010) 10319-10334.
[13] R.T. Mu, Z.J. Zhao, Z. Dohnalek, J.L. Gong, Structural motifs of water on metal oxide surfaces Chem. Soc. Rev. 46 (2017) 1785-1806.
[14] U. Diebold, The surface science of titanium dioxide Surf. Sci. Rep. 48 (2003) 53-229.
[15] A. Fujishima, X.T. Zhang, D.A. Tryk, TiO_2 photocatalysis and related surface phenomena Surf. Sci. Rep. 63 (2008) 515-582.
[16] M. Primet, P. Pichat, M.V. Mathieu, Infrared study of the surface of titanium dioxides. I. Hydroxyl groups J. Phys. Chem. 75 (1971) 1216-1220.
[17] C. Morterra, An infrared spectroscopic study of anatase properties .6. Surface hydration and strong lewis acidity of pure and sulfate-doped preparations J. Chem. Soc. Farad. T. 1 84 (1988) 1617-1637.
[18] K.S. Finnie, D.J. Cassidy, J.R. Bartlett, J.L. Woolfrey, IR spectroscopy of surface water and hydroxyl species on nanocrystalline TiO_2 films Langmuir 17 (2001) 816-820.
[19] C. Deiana, E. Fois, S. Coluccia, G. Martra, Surface Structure of TiO_2 P25 Nanoparticles: Infrared Study of Hydroxy Groups on Coordinative Defect Sites J. Phys. Chem. C 114 (2010) 21531-21538.
[20] L. Mino, G. Spoto, S. Bordiga, A. Zecchina, Particles Morphology and Surface Properties As Investigated by HRTEM, FTIR, and Periodic DFT Calculations: From Pyrogenic TiO_2 (P25) to Nanoanatase J. Phys. Chem. C 116 (2012) 17008-17018.
[21] C. Arrouvel, M. Digne, M. Breysse, H. Toulhoat, P. Raybaud, Effects of morphology on surface hydroxyl concentration: a DFT comparison of anatase-TiO2 and gamma-alumina catalytic supports J. Catal. 222 (2004) 152-166.
[22] S. Dzwigaj, C. Arrouvel, M. Breysse, C. Geantet, S. Inoue, H. Toulhoat, P. Raybaud, DFT makes the morphologies of anatase-TiO_2 nanoparticles visible to IR spectroscopy J. Catal. 236 (2005) 245-250.
[23] L. Mino, A. Zecchina, G. Martra, A.M. Rossi, G. Spoto, A surface science approach to TiO_2 P25 photocatalysis: An in situ FTIR study of phenol photodegradation at controlled water coverages from sub-monolayer to multilayer Appl. Catal. B-Environ. 196 (2016) 135-141.
[24] L. Mino, F. Pellegrino, S. Rades, J. Radnik, V.-D. Hodoroaba, G. Spoto, V. Maurino, G. Martra, Beyond Shape Engineering of TiO_2 Nanoparticles: Post-Synthesis Treatment Dependence of Surface Hydration, Hydroxylation, Lewis Acidity and Photocatalytic Activity of TiO_2 Anatase Nanoparticles with Dominant {001} or {101} Facets ACS Appl. Nano Mater. 1 (2018) 5355-5365.
[25] G. Busca, Spectroscopic characterization of the acid properties of metal oxide catalysts Catal. Today 41 (1998) 191-206.

[26] C. Binet, M. Daturi, J.C. Lavalley, IR study of polycrystalline ceria properties in oxidised and reduced states Catal. Today 50 (1999) 207-225.
[27] K.I. Hadjiivanov, D.G. Klissurski, Surface chemistry of titania (anatase) and titania-supported catalysts Chem. Soc. Rev. 25 (1996) 61-69.
[28] K. Hadjiivanov, J. Lamotte, J.C. Lavalley, FTIR study of low-temperature CO adsorption on pure and ammonia-precovered TiO_2 (anatase) Langmuir 13 (1997) 3374-3381.
[29] K. Hadjiivanov, B.M. Reddy, H. Knozinger, FTIR study of low-temperature adsorption and co-adsorption of (CO)-C-12 and (CO)-C-13 on a TiO_2-SiO_2 mixed oxide Appl. Catal. A-Gen. 188 (1999) 355-360.
[30] G. Martra, Lewis acid and base sites at the surface of microcrystalline TiO_2 anatase: relationships between surface morphology and chemical behaviour Appl. Catal. A-Gen. 200 (2000) 275-285.
[31] C. Deiana, G. Tabacchi, V. Maurino, S. Coluccia, G. Martra, E. Fois, Surface features of TiO_2 nanoparticles: combination modes of adsorbed CO probe the stepping of (101) facets Phys. Chem. Chem. Phys. 15 (2013) 13391-13399.
[32] L. Mino, A.M. Ferrari, V. Lacivita, G. Spoto, S. Bordiga, A. Zecchina, CO Adsorption on Anatase Nanocrystals: A Combined Experimental and Periodic DFT Study J. Phys. Chem. C 115 (2011) 7694-7700.
[33] L. Mino, G. Spoto, S. Bordiga, A. Zecchina, Rutile Surface Properties Beyond the Single Crystal Approach: New Insights from the Experimental Investigation of Different Polycrystalline Samples and Periodic DFT Calculations J. Phys. Chem. C 117 (2013) 11186-11196.
[34] J. Scaranto, S. Giorgianni, A quantum-mechanical study of CO adsorbed on TiO_2: A comparison of the Lewis acidity of the rutile (110) and the anatase (101) surfaces Theochem-J. Mol. Struct. 858 (2008) 72-76.
[35] J. Scaranto, S. Giorgianni, A DFT study of CO adsorbed on clean and hydroxylated anatase TiO_2 (001) surfaces Mol. Phys. 107 (2009) 1997-2003.
[36] A. Smekal, Zur Quantentheorie der Dispersion Naturwissenschaften 11 (1923) 873-875.
[37] C.V. Raman, K.S. Krishnan, A new type of secondary radiation 121 (1928) 501-502.
[38] G.S. Landsberg, L. Mandelstam, Eine neue Erscheinung bei der Lichtzerstreuung in Krystallen Naturwissenschaften 16 (1928) 557-558.
[39] R. Aroca, Surface-Enhanced Vibrational Spectroscopy, John Wiley & Sons, Ltd, 2007, pp. 73-106.
[40] R. Hara, M. Ishigaki, Y. Kitahama, Y. Ozaki, T. Genkawa, Excitation wavelength selection for quantitative analysis of carotenoids in tomatoes using Raman spectroscopy 258 (2018) 308-313.
[41] Q. Sun, C. Qin, Raman OH stretching band of water as an internal standard to determine carbonate concentrations 283 (2011) 274-278.
[42] N. Hayazawa, T.-a. Yano, S. Kawata, Highly reproducible tip-enhanced Raman scattering using an oxidized and metallized silicon cantilever tip as a tool for everyone 43 (2012) 1177-1182.
[43] R. Ossikovski, Q. Nguyen, G. Picardi, Simple model for the polarization effects in tip-enhanced Raman spectroscopy 75 (2007) 045412.

[44] E. Smith, G. Dent, Modern Raman Spectroscopy: A Practical Approach, Wiley, 2013.
[45] A.M. Rossi, S. Borini, L. Boarino, G. Amato, Lateral structuring of porous silicon: application to waveguides Phys. Status Solidi A-Appl. Mat. 197 (2003) 284-287.
[46] N.J. Everall, Confocal Raman Microscopy: Why the Depth Resolution and Spatial Accuracy Can Be Much Worse Than You Think 54 (2000) 1515-1520.
[47] H. Reinecke, S.J. Spells, J. Sacristán, J. Yarwood, C. Mijangos, Confocal Raman Depth Profiling of Surface-Modified Polymer Films: Effects of Sample Refractive Index 55 (2001) 1660-1664.
[48] Y. Maruyama, W. Kanematsu, Confocal volume in laser Raman microscopy depth profiling 110 (2011) 103107.
[49] S. Zakel, B. Pollakowski, C. Streeck, S. Wundrack, A. Weber, S. Brunken, R. Mainz, B. Beckhoff, R. Stosch, Traceable Quantitative Raman Microscopy and X-ray Fluorescence Analysis as Nondestructive Methods for the Characterization of $Cu(In,Ga)Se_2$ Absorber Films 70 (2016) 279-288.
[50] M. Valcarcel, A. Rios, E. Maier, A practical approach to metrology in chemistry and biology Accredit. Qual. Assur. 4 (1999) 143-152.
[51] D. Hutsebaut, P. Vandenabeele, L. Moens, Evaluation of an accurate calibration and spectral standardization procedure for Raman spectroscopy Analyst 130 (2005) 1204-1214.
[52] ASTM International, Standard Guide for Raman Shift Standards for Spectrometer Calibration, Designation: E 1840 – 96 (Reapproved 2002).
[53] B. Luo, X. Wang, M. Tian, Z. Cai, L. Li, Homogeneity quantification of nanoparticles dispersion in composite materials Polym Compos (2018).
[54] D.G. Wei, R. Dave, R. Pfeffer, Mixing and characterization of nanosized powders: An assessment of different techniques J. Nanopart. Res. 4 (2002) 21-41.
[55] H.C. Choi, Y.M. Jung, S.B. Kim, Size effects in the Raman spectra of TiO2 nanoparticles Vib. Spectrosc. 37 (2005) 33-38.
[56] G.A. Tompsett, G.A. Bowmaker, R.P. Cooney, J.B. Metson, K.A. Rodgers, J.M. Seakins, THE RAMAN-SPECTRUM OF BROOKITE, TIO2 (PBCA, Z=8) J. Raman Spectrosc. 26 (1995) 57-62.
[57] H.L. Ma, J.Y. Yang, Y. Dai, Y.B. Zhang, B. Lu, G.H. Ma, Raman study of phase transformation of TiO_2 rutile single crystal irradiated by infrared feratosecond laser Appl. Surf. Sci. 253 (2007) 7497-7500.
[58] C.J. Huberty, S. Olejnik, Applied MANOVA and Discriminant Analysis, Wiley, 2006.
[59] J.F. Hair, M. Sarstedt, C.M. Ringle, S.P. Gudergan, Advanced Issues in Partial Least Squares Structural Equation Modeling, SAGE Publications, 2017.